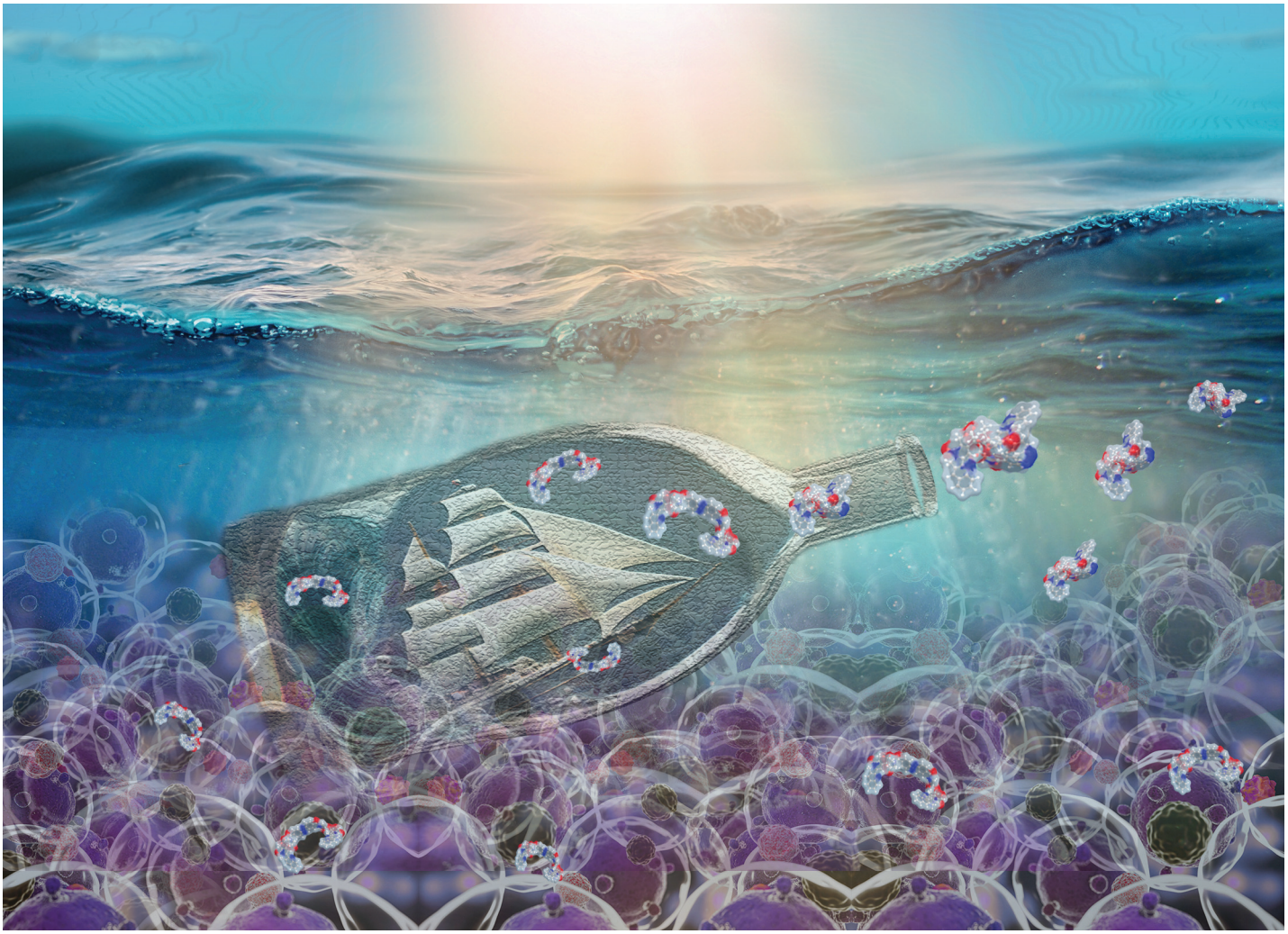

Dr. Botella's group at Nanomedicine Laboratory of Institute of Chemical Technology (Universitat Politecnica de Valencia-Spanish National Research Council) Valencia, Spain. Artwork by Katya Cuevas.

Light-activated controlled release of camptothecin by engineering porous materials: the *ship in a bottle* concept in drug delivery

A change in nanoparticle phototherapy is proposed by shifting photoswitching activity from the vehicle to the load. In this "ship in a bottle" concept, photoswitchable camptothecin containing an azobenzene functionality was loaded into porous silica nanoparticles with pores which limit its release when in the *trans* form. Release of the prodrug was accomplished by irradiation with UV light to convert trans isomers back to *cis*. This *cis–trans* photoisomerization allowed safe and precise delivery.

As featured in:

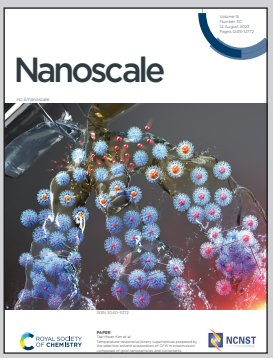

See Christopher C. Landry, Pablo Botella *et al.*, *Nanoscale*, 2023, **15**, 12506.

ROYAL SOCIETY OF CHEMISTRY

rsc.li/nanoscale

Registered charity number: 207890

Nanoscale

PAPER

View Article Online
View Journal | View Issue

Cite this: *Nanoscale*, 2023, **15**, 12506

Light-activated controlled release of camptothecin by engineering porous materials: the *ship in a bottle* concept in drug delivery†

Eva Rivero-Buceta, [a] Mirela E. Encheva, [b] Bradley Cech, [c] Eduardo Fernandez,[b] Germán Sastre, [a] Christopher C. Landry*[c] and Pablo Botella *[a]

Many systems for controlled drug release have been developed using different types of nanoparticles modified with azobenzene moieties. In these systems, drug release is often triggered by UV irradiation (either direct or using a near-infrared photosensitizer). These drug delivery systems often face challenges to their use, such as their lack of stability in physiological environments and concerns about their toxicity and bioavailability, that have hindered their translation from pre-clinical studies to clinical trials. Here, we propose a conceptual change by shifting photoswitching activity from the vehicle (nanoparticle) to the load (drug). In this "ship in a bottle" concept, the molecule to be delivered is trapped within a porous nanoparticle and its release is accomplished through a photoisomerization process. Using molecular dynamics, we designed and synthesized a photoswitchable prodrug of the antitumor drug camptothecin that contains an azobenzene functionality, and we have prepared porous silica nanoparticles with pore diameters designed to limit its release when in the *trans* form. Molecular modelling was used to show that the *cis* isomer was smaller and better able to pass through the pores than the *trans* isomer, which was confirmed by stochastic optical reconstruction microscopy (STORM). Thus, prodrug-loaded nanoparticles were prepared by loading the *cis* prodrug and then using UV irradiation to convert *cis* to *trans* isomers, trapping them, within the pores. Release of the prodrug was then accomplished by using a different UV wavelength to convert *trans* isomers back to *cis*. In this way, prodrug encapsulation and release could be achieved "on demand" through controlled *cis*–*trans* photoisomerization, which allowed the prodrug to be delivered safely and its release to be triggered precisely at the region of interest. Finally, the intracellular release and cytotoxic activity of this novel drug delivery system has been validated in several human cell lines, confirming the ability of this system to accurately control the release of the camptothecin prodrug.

Received 10th February 2023,
Accepted 31st May 2023

DOI: 10.1039/d3nr00642e

rsc.li/nanoscale

Introduction

Although nanomedicines are sometimes considered the drugs of the future, few of them have been used clinically in therapy or diagnostics.[1] They often face challenges that limit their translation from bench to bedside, including concerns about their stability in physiological media, selective accumulation in the region of interest (ROI), accurate and timely drug release, and elimination from the body.[2–5] In terms of nanomedicines designed to deliver chemotherapeutic drugs within tumors, efficient nanoparticle penetration into the tumor is a major issue. This is because insufficient blood supply, high-density cells and extracellular matrix, and increasing of interstitial fluid pressure can hinder the diffusion of the therapeutic load within the tumor. To overcome these limitations, several strategies have been proposed, including modulation of tumor microenvironment and optimization of nanoparticle physical properties.[6,7] In particular, improving the control of drug release is key to maximizing the performance of nanomedicines. To address this need, stimuli-responsive systems (SRSs) have been developed that provide accurate spatial and temporal control of molecular release, limiting undesired effects on healthy tissue and maximizing therapeutic activity in the ROIs.[8,9]

[a]*Instituto de Tecnología Química, Universitat Politècnica de València-Consejo Superior de Investigaciones Científicas, Avenida de los Naranjos s/n, 46022 Valencia, Spain. E-mail: pbotella@itq.upv.es*
[b]*Institute of Bioengineering, Universidad Miguel Hernández, Elche, Spain and Centre for Network Biomedical Research (CIBER-BBN), Avenida de la Universidad s/n, 03202 Elche, Spain*
[c]*Department of Chemistry, University of Vermont, 82 University Place, Burlington, VT 05405, USA. E-mail: Christopher.Landry@uvm.edu*

†Electronic supplementary information (ESI) available: Experimental details, including molecular dynamics methodology, prodrug synthesis and characterization, materials synthesis and characterization, drug loading and release, STORM methods, irradiation camera technology and biological validation. See DOI: https://doi.org/10.1039/d3nr00642e

Controlled molecular release has been accomplished in a variety of ways. For example, physical stimuli, such as magnetism, ultrasound irradiation, or light irradiation, have been used in SRSs to avoid any invasive effect over the surrounding tissue.[10,11] In particular, light-driven drug delivery systems (DDSs) can provide excellent local temporal control of drug release.[12] They are usually categorized into three groups: photothermal, photochemical, or photoisomerization-triggered systems.[13] The last category presents the clear advantage of reversibility, potentially allowing pulsed drug release, which is highly desirable from a clinical perspective. Among the light-driven DDSs, different chemical functional groups have been used in the design of light-switchable supramolecular structures, including spiropyran derivatives,[14] ligands containing 1,2-diethienylethene,[15] and azobenzene derivatives.[16] Indeed, azobenzene is the most frequently used photoisomerizable moiety for the development of DDSs due to its photochemical properties and ease of molecular construction. Azobenzene has two photoisomers, *e.g.*, *trans* and *cis* isomers, that can reversibly exchange by rotation across the –N=N– bond. Conversion from *trans* to *cis* conformation takes place under irradiation at wavelength of ~350 nm, while the conversion of *cis* to *trans* occurs under irradiation at ~450 nm. Many systems for controlled drug release have been developed using different types of azobenzene-modified nanoparticles, including polymers,[17,18] liposomes,[19] DNA,[20] metal organic frameworks (MOFs),[21] covalent organic frameworks (COFs),[22] and mesoporous silica.[23–25] These systems used UV irradiation, either of the azobenzene-containing substrate on its own or combined with a near-infrared (NIR) photosensitizer. The addition of a NIR component allows the use of tissue-penetrating NIR light in biological systems.

However, these DDSs are limited by the requirement to modify the nanoparticles' surfaces with specific functionalities, resulting in complex supramolecular structures that lead to nanoparticle aggregation in protein-containing physiological environments. This in turn decreases photosensitizing efficiency, leading to undesirable drug discharge, and ultimately results in rapid plasma clearance.[11] In addition, from a regulatory point of view, such hybrid materials face challenges including toxicity, bioavailability, pharmacokinetics, and others in translation from pre-clinical studies to clinical trials.[5]

One way to address these challenges is to shift the photoswitching activity from the vehicle (nanoparticle) to the load (drug). This strategy is especially well suited to a system using a porous nanoparticle. By tailoring the nanoparticle's pore diameter, molecular encapsulation and release is achieved "on demand" by activating and controlling *cis–trans* photoisomerization, provided that the stereoisomers have different molecular diameters. This "ship in a bottle" strategy (Fig. 1)[26] is a concept widely used in heterogeneous catalysis[27] but has been little used for drug delivery.[28–30]

In this work, we have extended the principle of "ship in a bottle" to the intracellular delivery and photo-activated release of an antitumor drug (camptothecin, CPT) by combining it with an azobenzene group and adsorbing it within mesoporous silica nanoparticles with tailored pore diameters. First, the design of this pro-drug was optimized using molecular dynamics, and the *cis* and *trans* isomers were adsorbed into custom-made cavities of silica nanoparticles. Then, the uptake of the isomers was examined by stochastic optical reconstruction microscopy (STORM), and their release was studied using *cis* ← → *trans* isomerization under UV irradiation. Finally, the intracellular release and cytotoxic activity of this novel DDS was evaluated in several human cell lines to confirm that the photoisomerization mechanism successfully controlled CPT release.

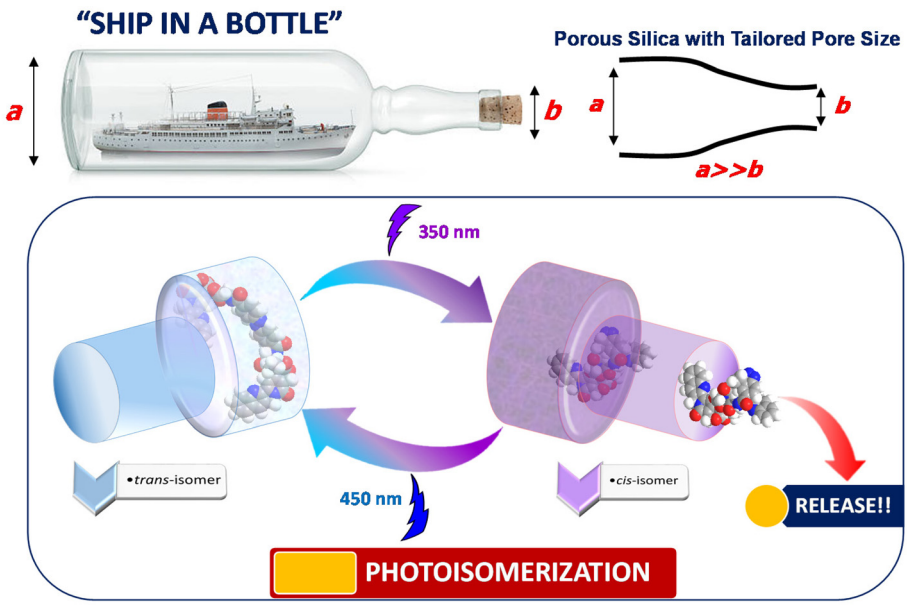

Fig. 1 Artistic scheme of the "ship in a bottle" concept and *cis–trans* photoisomerization as a drug-controlled release mechanism.

Experimental section

Molecular dynamics

Molecules. Three sets of camptothecin (CPT) derivatives were modelled that differed in the number of methylene (CH_2) groups inserted between the acetate and amide groups used to link azobenzene to CPT (Fig. 2). Each set consisted of *cis*/*trans* isomers.

A detailed description of the methods used for molecular dynamics calculations is given in the ESI.† Animations were recorded and are also available.

Preparation of bis(camptothecin glycinate)-4,4′-dicarboxylAzoBEnzene (CAABE)

The synthesis of camptothecin-20-*O*-glycinate was performed according to published procedures.[31] To a mixture of azobenzene-4,4′-dicarbonyl dichloride (I: 125 mg, 0.41 mmol) in anhydrous methylene chloride and dimethylformamide (48 : 2, 50 mL), camptothecin-20-*O*-glycinate (II: 373 mg, 0.92 mmol) and TEA (0.13 mL) were added. The reaction was stirred overnight at room temperature under inert atmosphere. The resulting suspension was filtered and the supernatant was concentrated in a rotary evaporator to obtain an orange oil. This residue was purified by two or three cycles of trituration with ethyl acetate, methanol and ether (in various combinations) to give CAABE (III) as an orange solid (yield: 32%). The CAABE synthesis scheme and characterization protocols are shown in the ESI.†

Preparation of large pore-mesoporous silica nanoparticles (LSN)

Mesoporous silica nanoparticles with large pores (LSN) were synthesized following the low temperature method previously described by our group.[4,32] Briefly, 0.25 g of F127 surfactant and 0.70 g of FC4 surfactant were dissolved in 30 mL of and aqueous solution of HCl (0.02 M). Then, 0.23 mL of 1,3,5-trimethylbenzene was added and the mixture was stirred at 10 °C for 2 h. Tetraethyl orthosilicate (TEOS, 1.6 mL) was then added to the solution and stirring was continued at 10 °C for 24 h. The final molar ratio of the reactants TEOS/F127/TMB/FC4/HCl/H_2O was 1 : 0.0028 : 024 : 0.12 : 0.08 : 232. The reaction mixture was then transferred to an autoclave and hydrothermally treated at 135 °C (LSN-1) or 150 °C (LSN-2 and LSN-3) for 24 h. The resulting suspension was cooled, filtered, and washed with water and ethanol. In the case of LSN-3, a second hydrothermal treatment was performed. For this purpose, 0.50 g of LSN-3 was placed in an autoclave and hydrothermally treated at 140° C for 48 h. Finally, the template was removed by digestion in a microwave unit (microwave irradiation over MARS-5 at 800 W, 2245 MHz, and 220 V).[33] Methods for materials characterization are described at the ESI.†

Photoisomerization, drug loading and drug release

***cis–trans* photoswitching.** The optical absorbance spectra of CAABE derivatives were measured using a Photon Technology International (PTI, Germany) LPS-220B spectrofluorometer equipped with a 75 W xenon lamp and a monochromator in the wavelength range 200–700 nm. Samples were irradiated in a 1 cm path length quartz cuvette at 73 mW cm^{-2} with agitation. To study photoswitching, a solution of *trans*-CAABE (1 mg mL^{-1}) in a mixture DMSO : ethanol (1 : 4 v/v) was irradiated at 350 nm. Absorption spectra were recorded immediately after irradiation in a Cary 50 UV-Vis (Varian) spectrophotometer. When the *trans* → *cis* photoswitching reached equilibrium, the solution was irradiated at 450 nm and the absorption spectra corresponding to the *cis* → *trans* transformation were recorded immediately after irradiation. The photoisomerization quantum yield (*R*, also named photoisomerization degree at the photostationary state) was determined using eqn (1):

$$R = |A_0 - A_t|/|A_0 - A_\infty| \times 100 \quad (1)$$

where A_0 is the initial absorbance at 0, A_t is the absorbance at time *t*, and A_∞ is the absorbance at equilibrium.

Drug loading. To adsorb *trans*-CAABE into LSN, a solution of *trans*-CAABE (1 mg mL^{-1}) in a mixture DMSO : ethanol (1 : 4 v/v) was incubated in a 1.5 mL Eppendorf tube with 5 mg of LSN (RT, 1500 rpm, 24 hours). Subsequently, the reaction mixture was centrifuged (16 100*g*, 12 min) and the supernatant decanted. The remaining pellet was washed with 1 mL of methanol and 1 mL of water. Adsorption of *cis*-CAABE into LSN took place in full darkness. A solution of *cis*-CAABE (1 mg mL^{-1}) in a mixture DMSO : ethanol (1 : 4 v/v) was irradiated at 350 nm for two hours to insure the complete conversion of *trans* to *cis* isomer prior to adsorption. This mixture was sub-

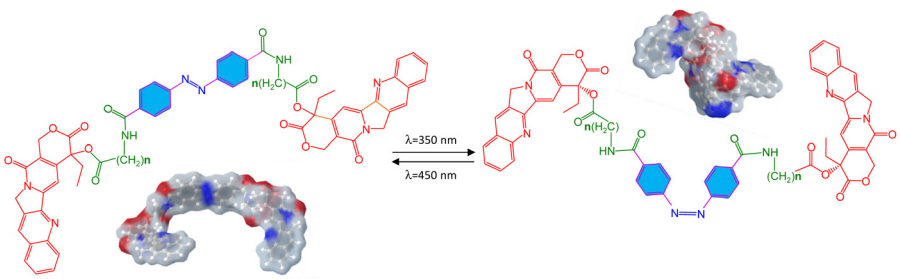

Fig. 2 *Trans* (left) and *cis* (right)-CAABE derivatives (*n* = 0, 1, or 2). The results of 3D Conolly molecular simulations using the CAABE derivative with *n* = 1 are shown as insets. The abbreviation CAABE is defined below.

sequently incubated in a 1.5 mL Eppendorf tube with 5 mg of LSN (RT, 1500 rpm, 24 hours). Then, the mixture was centrifuged (16 100*g*, 12 min) and the supernatant decanted. The remaining pellet was washed with 1 mL of methanol and 1 mL of water.

Drug release. To study the photo-triggered release of CAABE, LSN-1 nanoparticles loaded with *cis*-CAABE (5 mg) were suspended in 1 mL of Milli-Q water and irradiated at 450 nm for one hour to convert *cis*- to *trans*-CAABE. Then, the suspension was centrifuged (16 100*g*, 12 min) and the supernatant was discarded. The solid was then re-suspended in 1 mL of Milli-Q water and incubated at 37 °C for various times. The aliquots from the incubations were centrifuged (16 100*g*, 15 min) and the supernatants were discarded. Pellets were then incubated in a NaOH solution (0.05 N) and shaken at 1500 rpm for 3 hours at 37 °C. After decanting the supernatant, the remaining pellet was freeze-dried and then reconstituted with 1 mL of a mixture MeOH : HCl 95 : 5 (v/v). Free CPT in the solution was quantified by Reverse-Phase High Performance Liquid Chromatography (RP-HPLC). For comparison, the release of *cis*-CAABE was also studied, again in full darkness. *cis*-CAABE/LSN-1 nanoparticles (5 mg) were suspended in 1 mL of Milli-Q water and irradiated at 350 nm for two hours to insure all *trans* isomer was converted to *cis*-CAABE. The same procedure described above was then followed. RP-HPLC methods for CPT quantification are described in the ESI.†

Internal diffusion of CAABE *cis*/*trans* isomers studied by STORM

A study by Stochastic Optical Reconstruction Microscopy (STORM) was performed using LSN-1 nanoparticles after adsorption of *cis*-CAABE or *trans*-CAABE molecules. Drug loading was performed using the protocols described above. LSN-1 particles loaded with either *cis* or *trans* CAABE were excited using a 405 nm laser, and a minimum of 7500 frames were collected for each run. All molecules with a minimum peak height greater than 300 were considered for further analysis in NIS-Elements. For the data analysis and reconstruction several ROIs were created to isolate data specific to individual spheres, from which Cartesian coordinates of the detected molecules were extracted to .txt files for data reconstruction.

Penetration depths of each molecule into the sphere were determined by calculating the difference between the distance of each molecule from the sphere center and the calculated radius of the sphere. Averaging the penetration depths for each respective sphere yielded the mean penetration depth. The total number of molecules within a sphere was found by counting the number of Cartesian coordinates detected by STORM. Using the transformed Cartesian coordinates of each molecule and the sphere of best fit, a 3D model of each sphere was reconstructed using Blender modeling software. A Python code was written to import the molecule coordinates and construct a wire-frame sphere to reflect what was imaged *via* STORM. Movies showing a full 360° view of each sphere were exported as .mp4 files. Additional details on the STORM methods are provided in the ESI.†

Biological validation

***In vitro* assays.** The effect of CAABE/LSN-1 nanoparticles on cell metabolic activity was evaluated by using the 3-(4,5-dimethylthiazol-2-yl)-5-(3-carboxymethoxyphenyl)-2-(4-sulfophenyl)-2*H*-tetrazolium (MTS) colorimetric assay. The cytotoxicity of CAABE (IC_{50} value) has previously been determined and compared to that of free CPT (see ESI†). For the experiments performed as part of the current study, cells were seeded in 96-well plate at a density of 4500 (HeLa) or 8000 (U251, SH-SY5Y) cells per well and incubated in 5% CO_2 at 37 °C for 24 h. Then, cells were exposed for 24 h to CAABE/LSN-1 nanoparticles at two different prodrug concentrations: 0.16 and 0.48 μg mL^{-1}, which correspond to 0.10 and 0.32 μg mL^{-1} of CPT. All dilutions were prepared in cell culture medium. The 96-well plate was then placed in a hand-crafted camera and irradiated at 350 nm (2.2 mW cm^{-2}) for 30 or 60 min. A scheme and picture of the irradiation camera are shown in Fig. 3, and full description and additional images of this device are shown in the ESI (Video SV-1†). After irradiation, cells were incubated for an additional 72 h. Then, 10 μL of MTS solution (5 mg mL^{-1}) in cell culture medium was added to each well and incubation was continued for 4 h. The supernatant in each well was then carefully removed and 150 μL of isopropanol was added to dissolve formazan crystals. Absorbance was measured with a PerkinElmer Wallac 1420 VICTOR2 Multilabel HTS Counter (Northwolk, CT, US) at the wavelength of 570 nm. Six independent experiments were performed at each drug concentration (n = 6), and each experiment was carried out in biological triplicate. Controls with no nanoparticles and no irradiation were also performed. Absorbance values were normalized with respect to the controls, and expressed as percentage by using eqn (2):

$$\text{Relative cell viability} = \frac{\text{OD}_{595}\ \text{test sample}}{\text{OD}_{595}\ \text{control}} \times 100. \qquad (2)$$

Finally, additional control experiments testing the biocompatibility of CAABE-free nanoparticles, with and without irradiation, were also performed. Details of these experiments are in the ESI.†

Statistics

Cell viability mean and corresponding standard error of the mean (SEM) values were determined for each experiment, and results were presented as the mean ± SEM. Data were compared by the unpaired Student's t-test. Significant differences among the groups were calculated at $p < 0.05$ or less. All the analysis and graphs were carried out by using GraphPad Prism 6 software (GraphPad Software, San Diego, CA, USA).

Results and discussion

Molecular dynamics

Analysis of the structures obtained after 300 ps molecular dynamics simulations (Fig. 4) allowed us to plot the histograms of C–N=N–C dihedrals, to determine whether the iso-

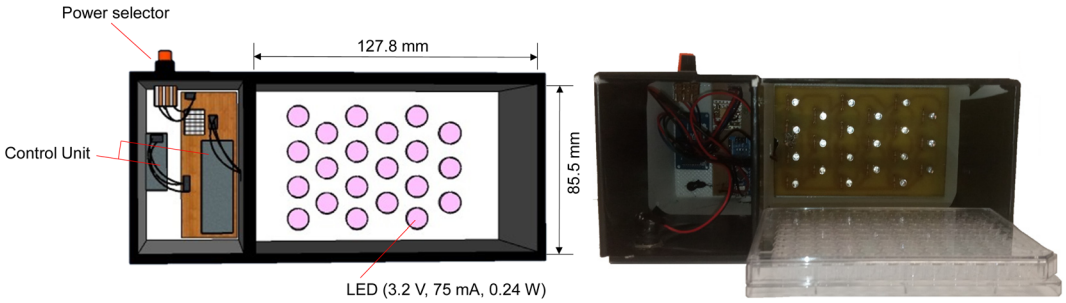

Fig. 3 Hand-crafted irradiation camera used in the *in vitro* photoisomerization experiments. (a) Scheme of functional components (front view); (b) real experimental device with a 96-well plate.

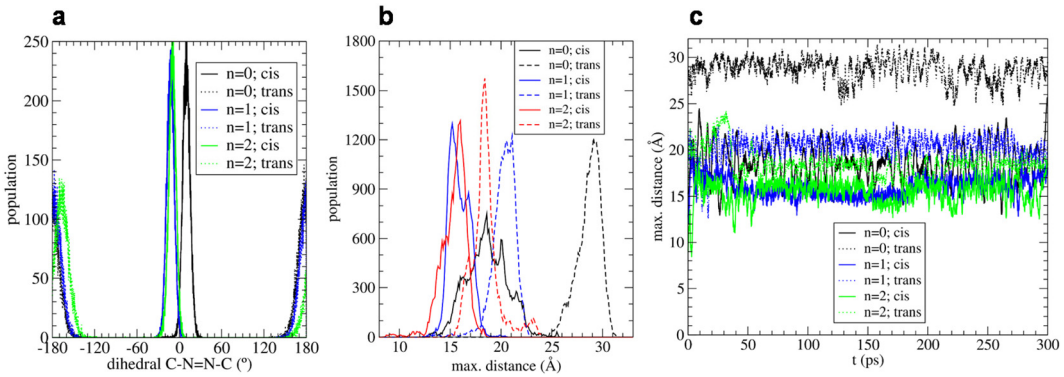

Fig. 4 (a) Histogram of C–N═N–C dihedrals in the three sets of *cis–trans* azobenzene isomers ($(CH_2)_n$, n = 0, 1, or 2) resulting from 300 ps molecular dynamics simulation. (b) Histograms of the maximum distance between pairs of atoms in the three sets of isomers. This maximum distance has been defined to account for molecular size. (c) Maximum distance during the simulation between pairs of atoms in the isomers.

meric configurations were retained during the simulation. While the *trans* isomer is considerably more stable and should remain structurally intact during simulation, one could expect the *cis* isomer to isomerize because experimental data showed that it is only stable upon irradiation. Simulation of the *cis* isomer was performed largely by increasing the dihedral constant to prevent relaxation to the *trans* isomer. Fig. 4a confirms that the isomer type was retained throughout the simulation. For the *trans* isomer, the C–N═N–C dihedral angle showed maxima at 180° and −180°, ±30°. However, the *cis* isomer did not have the anticipated maximum at a dihedral angle of 0°, due to short-range repulsions between molecule moieties at either side of the C–N═N–C dihedral. Instead, maxima at ~15° and −15° are found with symmetric distributions for each *cis*-molecule.

Considerable folding was observed for each molecule during the 300 ps of simulation time. A large number of configurations are possible, most of them allowed by the small energetic penalty associated with many of the dihedral angles present in the molecule. This strongly influenced the effective size of the molecule which, in turn, limited its ability to enter the pores of LSN. To study the effective molecular size, several interatomic distances were defined in each molecule using a program to identify the two most distant pairs of atoms in the molecule during the molecular dynamics simulation (Fig. S1, ESI†). The corresponding histograms of maximum distances are shown in Fig. 4b. For all sets of dimers studied (that is, 0, 1, or 2 CH_2 groups in the CPT-azobenzene link), the effective molecular size was larger in the *trans* isomer than in the corresponding *cis* isomer, and the size difference between isomers became smaller in the series $(CH_2)_n$ as n increased from 0 to 2. This was due to the fact that the larger molecules, with more degrees of freedom, have a larger capability to fold, so the larger initial size of the *trans* isomer can be reduced by rotation around an increasing number of dihedrals. When considering molecular design parameters for the ship-in-a-bottle concept, the absolute molecular sizes of the isomers and the difference in size are both important. Fig. 4b shows that the average molecular sizes and differences (in Å), respectively for *cis*/*trans* are: 18.6/28.7, Δ = 10.1 (n = 0); 15.8/20.5, Δ = 4.7 (n = 1), and 15.5/18.2, Δ = 2.7 (n = 2).

Movies of molecular structure changes during the simulations (Videos SV2–SV7, ESI†) showed that the molecules were partially unfolded only during the initial stages of the simulations. As the simulations progressed, the conformational energy can be reduced through van der Waals interactions, and folding occurred. Folding was always more effective for the *cis* isomers, although at n = 2 the difference between *cis*

and *trans* isomers was almost negligible. As a consequence, the effective molecular size of the *cis* isomers was always smaller than the *trans* isomers. Fig. 4c highlights this conclusion, where the molecular size at each conformation was plotted during the simulation time.

Preparation of CAABE and photoisomerization

The key parameters in the selection of the CAABE derivative to be used in our drug delivery system are molecular size and degrees of freedom. In this context, the derivative with $(CH_2)_n$ where n = 0 appeared to be the best candidate to perform the photoisomerization and loading/release assays with nanoparticles. Unfortunately, all attempts to synthesize the n = 0 CAABE derivative were fruitless, as this compound is quite sterically hindered. However, synthesis of CAABE with n = 1 and n = 2 was successful. The synthetic steps and chemical structure of the n = 1 compound are shown in Fig. S2.† CPT was substituted at 20-OH position with glycine through an ester bond,[31] and the resulting molecule was covalently attached to diazobenzene through amide bond formation between the glycine and acid chlorides on the diazobenzene. The ^{1}H-NMR spectrum of *trans*-CAABE (Fig. S3†) shows the protons of the diazobenzene group as a multiplet along with CPT protons around 7.94 and 8.16 ppm. Peaks in the ^{13}C-NMR spectrum at 167.05 and 165.85 ppm (Fig. S4†) were assigned, respectively, to the ester bond between the glycine and the CPT hydroxyl and to the amide bond between CPT and diazobenzene (Fig. S2†). In the 2D-COSY spectra (Fig. S5†), CAABE was identified by the signal of the glycine methylene protons between 4.14 and 4.47 ppm and their correlation with the proton of the amide group at 9.32 ppm. On the other hand, CAABE HSQC spectrum (Fig. S6†) allowed the chemical shift of each proton to be directly correlated to the chemical displacement of its corresponding carbon. Finally, the molecular weight of CAABE was confirmed by high resolution mass spectrometry (HRMS, Fig. S7†). In addition, for the purpose of comparison, the most relevant structural features of the n = 2 derivative (CAABE-2) are shown at the revised ESI (Fig. S8–S10†).

The photoswitching property of diazobenzenes between *cis* and *trans* isomers is well known.[34–36] In these experiments, the photoisomerization of CAABE was confirmed by UV-Vis spectroscopic studies in solution. The spectrum of *trans*-CAABE before irradiation (Fig. 5a) featured a band at 347 nm (π–π^* transition) and a weak band at 444 nm (n–π^* transition). Upon UV light irradiation (350 nm), the absorption band at 344 nm gradually decreased while a band at 450 nm increased, indicating CAABE *trans* → *cis* photoisomerization. These spectral changes could be reversed by irradiation at 450 nm, indicating CAABE *cis* → *trans* photoisomerization (Fig. 5b) and reversibility. In the isomerization under UV light there were two isosbestic points at 347 and 394 nm, while in the process under visible light the only isosbestic point emerged at 394 nm.[37]

The photoisomerization quantum yield (R) of the photoisomerization process was determined by irradiating CAABE for various lengths of time and performing the calculation shown in eqn (3). Upon irradiation at 350 nm, the equilibrium absorbance (A_∞) corresponding to completion of photoswitching was reached at 116 min; when 450 nm light was used, photoswitching was completed at 10 min (Fig. S11, ESI†). This can be explained by the faster kinetics of *cis* → *trans* compared to the *trans* → *cis* transformation, which is consistent with the greater stability of the *trans* isomer.

Preparation of LSN materials, drug loading and drug release

LSN with tailored pore entrances and internal cavities were obtained by a low temperature method and using a dual surfactant system (Pluronic F127 and FC4).[4,32,38] The most significant physico-chemical properties of these materials are summarized in Table 1.

N_2 physisorption measurements showed type IV adsorption–desorption isotherms with an H2-type hysteresis loop in LSN-1 and LSN-2. LSN-3 showed an H3-type hysteresis loop as a consequence of the dramatic enlargement of the entrance size (Fig. S12†). As expected, BET surface area decreased with the enlargement of pore diameter. Transmission electron

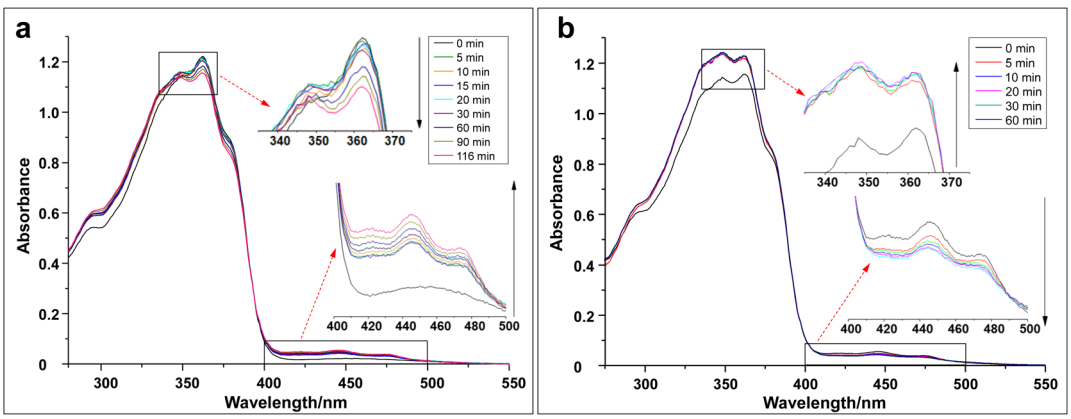

Fig. 5 UV-Vis spectra of CAABE after irradiation. (a) Irradiation at 350 nm for the *trans* → *cis* photoisomerization. (b) Irradiation at 450 nm for the *cis* → *trans* conversion. The insets detail the absorbance spectra changes with irradiation time.

Table 1 Physico-chemical properties of as-synthesized materials

Sample	Particle size[a] (nm)	Cavity size[b] (nm)	Entrance size[c] (nm)	S_{BET} (m^2 g^{-1})	V_p (cm^3 g^{-1})
LSN-1	149.6 ± 46.7	15.5	4.2	616.9	0.85
LSN-2	171.4 ± 61.4	13.6	7.2	429.2	0.80
LSN-3	160.6 ± 75.9	13.8	12.0	292.6	0.81

[a] Determined from TEM measurements over a minimum of 100 particles. [b] Calculated from the adsorption curve of the N_2 sorption isotherm, based on the BJH method. [c] Calculated from the desorption curve of the N_2 sorption isotherm, based on the BJH method.

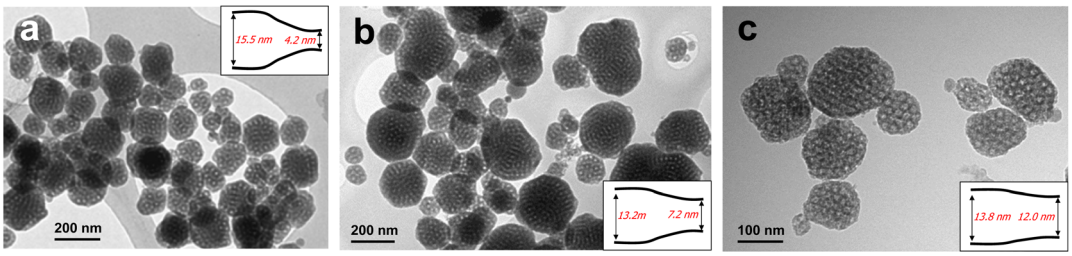

Fig. 6 TEM images of large pore mesoporous silica nanoparticles with different pore diameter shown in the insets. (a) LSN-1. (b) LSN-2. (c) LSN-3.

microscopy (TEM) images of LSN materials showed in all cases highly monodisperse nanoparticles (Fig. 6).[4] Particle size distribution ranged from 70 to 300 nm, with a similar mean size in the three samples (149–171 nm). The particle diameters measured by dynamic light scattering (DLS) were slightly larger than those observed by TEM, indicating the presence of some particle dimers and oligomers in the suspension (see ESI and Fig. S13†).

Drug loading is a key step in the development of novel nanomedicines, as it determines both the intrinsic activity of the drug delivery system and its ability to deliver its payload to the target cells while avoiding nonspecific release.[2] In the case of porous materials, synthetic control of the pore diameter is crucial to optimizing the loading and release rates of the delivered drug, as has been previously reported for mesoporous silica.[39] This is extremely important in the case of CPT, as a variety of negative effects (low water solubility, pronounced loss of activity from lactone-ring hydrolysis, and severe toxicity), strongly limit its clinical use.[40] In this study we have designed LSN materials to enhance CAABE loading by modifying the pore entrances of mesoporous silica nanoparticles. As described above, according to molecular dynamics calculations the average molecular size ratio of the *cis*/*trans* isomers of CAABE ($(CH_2)_n$, n = 1) was 15.8/20.5 (Å). On this basis, both isomers could be expected to diffuse within the internal cavities of the LSN, where the pore diameter was 13 to 15 Å. However, pore entrances should impose a bottleneck (diameters 4–7 nm for LSN-1 and −2, Table 1) that could be used to discriminate *cis* and *trans* isomers based on their rates of diffusion. Here, LSN were incubated with a solution of either *cis* or *trans* CAABE with $(CH_2)_1$ and the amount of adsorbed compound was determined by elemental analysis. The results (Table 2) show that LSN-1, with the smallest pore entrance, adsorbed nearly 7 times as much of the *cis* isomer as the *trans* isomer. In contrast, LSN-2 and -3, with larger pore entrances, allowed more diffusion of the *trans* isomer leading to equal or nearly equal adsorption of both isomers. The smaller mass of both CAABE isomers adsorbed by LSN-3 is related to the lower surface area of this material.

Table 2 Incorporation of n = 1 CAABE *cis*–*trans* isomers into LSN materials[a]

Sample	Pore/cavity size[b] (nm)	*cis*-CAABE (wt%)	*trans*-CAABE (wt%)	*cis*–*trans* ratio
LSN-1	4.2/15.5	2.0	0.3	6.7
LSN-2	7.2/13.6	2.2	1.1	2.0
LSN-3	12.0/13.8	0.5	0.7	0.7

[a] Determined by elemental analysis. [b] Determined by the BET-BJH method from the N_2 adsorption–desorption isotherms.

The ability of LSN-1 particles to adsorb more of the *cis*-CAABE isomer with $(CH_2)_n$ (n = 1) was also confirmed by stochastic optical reconstruction microscopy (STORM). In this technique, photoswitchable fluorophores are manipulated to stochastically turn on and off, and the STORM instrument records these "blinks" through numerous cycles. Because the position information of each fluorophore is collected in a database, reconstruction of the image and calculations based on the position information are possible. We recently demonstrated the utility of STORM in addressing questions about molecular adsorption in porous materials. In that work, we used STORM to compare the penetration depth of fluorescently labelled proteins with different sizes within silica nanoparticles that had pores with the same diameter. Here, we apply STORM to investigate the penetration depth of the *cis*/*trans*-CAABE isomers within LSN-1 particles.

LSN-1 particles were loaded with CAABE isomers by stirring the particles in a solution containing 1 mg mL^{-1} CAABE and 5 mg mL^{-1} LSN-1 nanoparticles. Upon excitation at 405 nm in the STORM instrument, emission of the isomers was observed and collected. Several particles were selected for analysis and fluorophore information associated with the particles were extracted as Cartesian coordinates. This information was used to calculate the sphere of best fit in each case, by minimizing the function shown in eqn (SE3) in the ESI.† This allowed us to identify the relative locations of each CAABE molecule within the particle. With this information, reconstructed images were produced from the STORM shown in Fig. 7a (*cis*) and Fig. 7b (*trans*). It is qualitatively apparent from these images that a larger amount of the *cis* CAABE isomer was present in the LSN-1 particles than the *trans* isomer. Another view of the information (Fig. 7c and d) was created by taking an optical slice through the data set, and flattening the information into one layer by plotting as a function of x and y. Both views confirm that significantly more of the *cis* isomer was found within the nanoparticle than the *trans* isomer. Quantitative analysis, summarized in Table 3, was also performed by summing the number of molecules identified in the STORM analysis within the calculated perimeter of the

Table 3 Fluorophore count within LSN-1 particles loaded with CAABE isomers, determined by STORM

	cis-CAABE loaded in LSN-1	*trans*-CAABE loaded in LSN-1
Fluorophore count	984	194

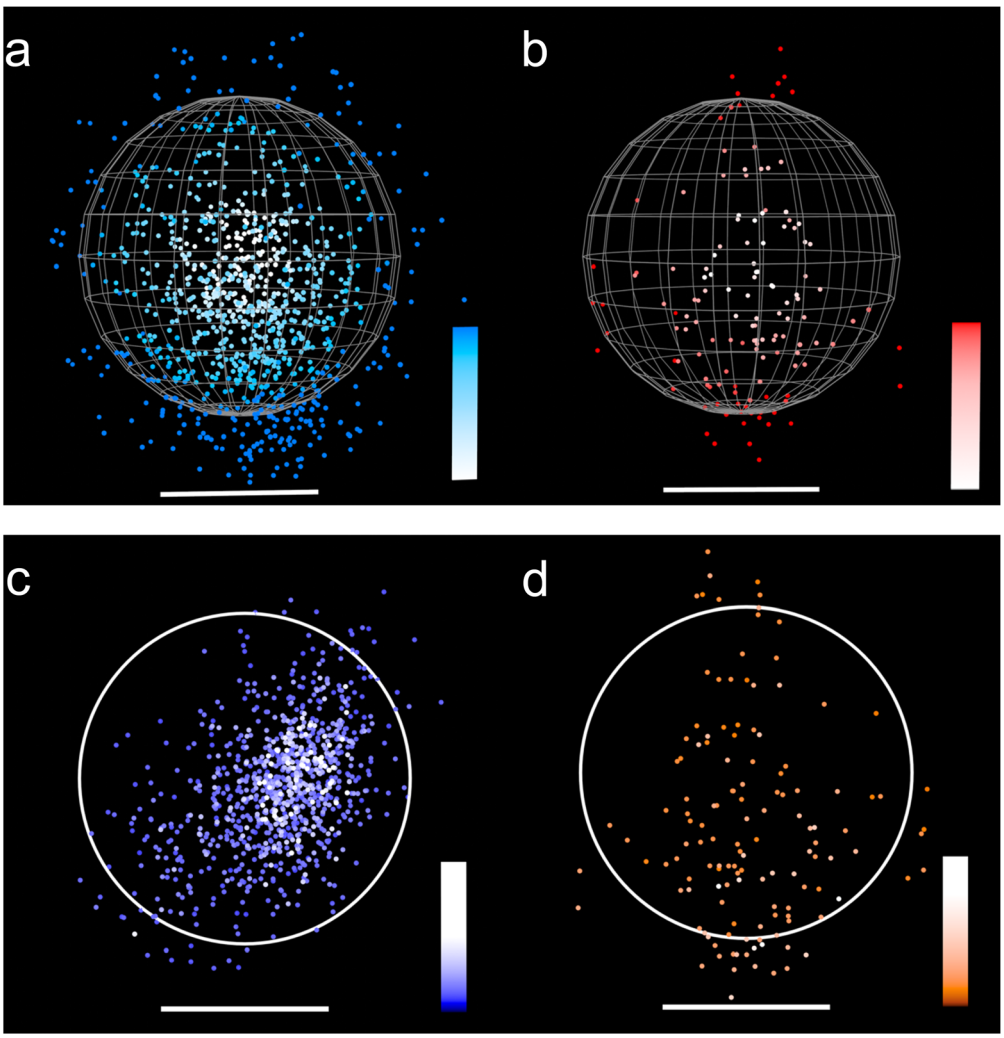

Fig. 7 Representative STORM images of CAABE isomers after adsorption within LSN-1 particles. *cis* molecules are shown in (a) and (c), and *trans* molecules are shown in (b) and (d). *Top row*: a mesh outline of a particle was created from the position information of the molecules within a particle in each sample, and then molecular positions were plotted as a function of their (x,y,z) coordinates. Lighter tones indicate deeper penetration within the particle. *Bottom row*: an optical slice was taken through the data, and then the information was "flattened" by plotting in the (x,y) plane as a function of fluorescence intensity. In this plot, lighter tones indicate stronger fluorescence. Bar = 200 nm.

sphere. Five times as many fluorophores were identified in LSN-1 particles loaded with the *cis* isomer compared to the *trans* isomer. Additional movies showing this fact are provided at the ESI (Videos SV8–SV11†). These results are similar to our previous experiments using proteins of various sizes to examine adsorption within porous silica nanoparticles.[41] We found a close relationship between the pore diameters of the nanoparticles and the sizes of the proteins found in their adsorbed protein coronas. In these studies, the smaller diameter of the *cis* isomer allows it to penetrate deeper into the LSN-1 particles.

Using drug loading and internal diffusion data from elemental analysis and STORM, we then investigated the controlled release of CAABE from LSN-1 in water, triggered by UV-Visible light irradiation. For these studies, drug-loaded LSN-1 were irradiated at either 350 nm for two hours (for release of the *cis* isomer) or 450 nm for one hour (for release of the *trans* isomer), and CPT concentration in solution was measured by RP-HPLC.

Fig. 8 highlights the impact of the LSN-1 pore structure on the diffusion of *cis vs. trans* CAABE isomers. From the start of the experiment, *trans* isomer is clearly released at a slower rate than the *cis* isomer, and the maximum amount that can be released is nearly complete after only one hour. In contrast, the *cis* isomer showed a faster initial release rate than the *trans* isomer, and the amount released continued to increase for more than six hours. The total amount of CAABE released was approximately three times higher for the *cis* isomer. According to STORM data, the release of the *cis* isomer is expected to occur from the whole mesoporous silica matrix, whereas *trans*-CAABE should diffuse outside the particle only from the most external layers, with the majority of the drug loading remaining at the core (Fig. 8). This highlights the effectiveness of the "ship in a bottle" mechanism in establishing control over release of the CAABE dimer through photoisomerization, leading to the potential application of this system in biological medium. A former approach to the loading of topotecan into a mesoporous structure by a "ship in a bottle" mechanism was carried out in MIL-100 nanoMOFs, although in this case drug liberation was not subjected to specific stimuli.[28] To the best of our knowledge, this is first description of a DDS linking "ship in a bottle" drug loading and *cis* ← → *trans* photoisomerization-driven release.

The release patterns of the *cis* and *trans* CAABE diastereoisomers from LSN-1 fit very well into Higuchi's square root model shown in eqn (3) (Table 4, and Fig. S14†).

$$X = k_H \cdot t^{\frac{1}{2}} \quad (3)$$

In this equation, X, t, and k_H are, respectively, the fraction of discharged drug, release time, and the kinetic constant.[42,43] Here, the comparison of k_H values for the *cis*- and *trans*-CAABE showed the same ratio observed at the end of liberation process ($k_{Hcis} \sim 3$ fold k_{Htrans}). This means that diffusion plays the dominant role in defining the release rate, with very little contribution from material degradation. This is consistent with the low water solubility of CAABE and the stability of the silica matrix in aqueous conditions.[44]

Biological validation

The potential therapeutic use of the photo-activated DDS described above was evaluated using three commercial cancer cell lines (SH-SY5Y, U251, HeLa) with similar growth rates (doubling times of 25–30 h),[45–47] to avoid inconsistencies related with the overgrowth of an specific cell line after irradiation. CAABE and CPT cytotoxicity was validated using the MTS assay in HeLa cells (Fig. S15†), showing similar IC_{50} values, which confirms full hydrolysis of the prodrug into the cytosol through enzymatic activity.[40] The biocompatibility of

Table 4 Kinetic parameters of Higuchi's kinetic model for the *cis*/*trans*-CAABE release in LSN-1 material after photoisomerization with UV-Vis light in water, at 37 °C [a]

Sample	Drug loading (wt%)	Interval (min)	k_H [a] ($h^{1/2}$)	r [b]
trans-CAABE	2.0	0–15	36.90	0.9961
cis-CAABE	2.0	0–15	90.93	0.9941

[a] Higuchi's release constant. [b] Regression coefficient.

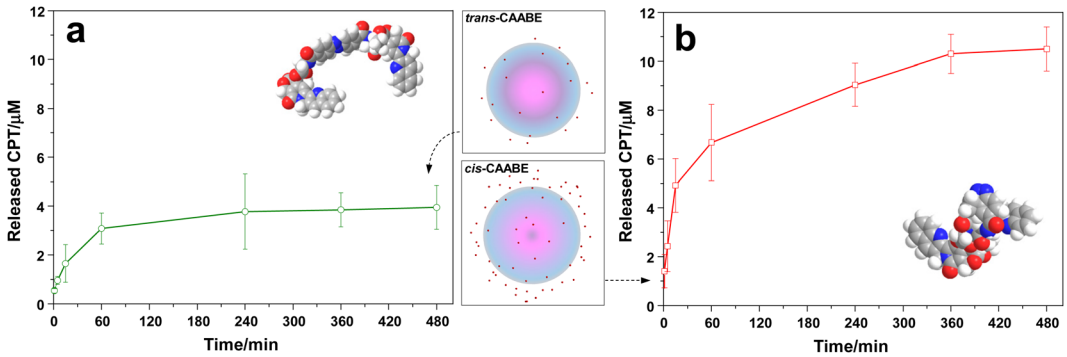

Fig. 8 Cumulative release profiles of *trans*-CAABE (a) and *cis*-CAABE (b) isomers from LSN-1 nanoparticles after photoisomerization by UV-Vis light in water, at 37 °C. The insets at the middle are artistic representations of the liberation process through the mesoporous silica matrix.

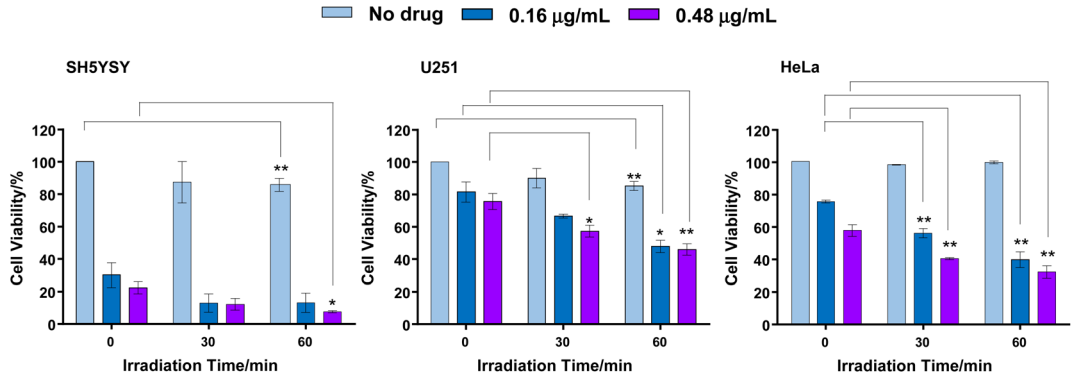

Fig. 9 *In vitro* cytotoxicity assay using SH-SY5Y, U251 and HeLa cells incubated 24 h with CAABE/LSN-1 nanoparticles at two different prodrug equivalent concentrations (0.16 or 0.48 μg mL^{-1}) (n = 6). Photoexcitation was performed with UV light (350 nm, 2.2 mW cm^{-2}) for 30 or 60 min and followed by incubation for additional 72 h. Controls correspond to cells with CAABE-free nanoparticles (no drug), and/or cells that were not irradiated. Experiments were performed in triplicate, and the results are shown as the mean ± SEM. Statistical differences were determined by employing the unpaired Student's t-test between the obtained data (*e.g.* 30 min/0.16 μg mL^{-1}) and the corresponding control (*e.g.*, 0 min/0.16 μg mL^{-1}). Significant differences among the groups were calculated at $p < 0.05$ (*) or at $p < 0.01$ (**).

LSN-1 was tested in all cell lines in a wide range of concentrations (Fig. S16†), with no significant cytotoxicity observed under our experimental conditions. We also confirmed that CAABE-loaded LSN-1 is not cytotoxic during the first 24 h incubation step (*i.e.*, prior to irradiation) by repeating the MTS assay in each cell line and using CAABE/LSN-1 concentrations up to the maximum amount used in the irradiation experiments (0.48 μg mL^{-1} prodrug equivalent concentration). No significant decrease in cell viability was observed in these control experiments (Fig. S17†). This is because *trans*-CAABE is trapped within LSN prior to UV irradiation (Fig. 8). Moreover, we previously showed that CPT-loaded silica nanoparticles induce cell cycle arrest in G2/M phase in response to DNA damage comparable to that observed with the naked drug. This cytotoxicity mechanism requires a longer incubation time (about 48–72 h) to initiate cell apoptosis.[48] In addition, some long-term *in vivo* studies have shown that silica nanoparticles may lead to chronic toxicity, mostly liver inflammation.[49] Even in those studies, however, mesoporous silica nanoparticles showed a safer toxicological profile than solid, Stöber-like, silica nanoparticles due to their higher hydrolytic susceptibility and faster plasma clearance. Our data confirmed their potential use in clinical translation as drug delivery vehicles.

Fig. 9 shows quantitative measurements of cell viability using the MTS assay after 24 h incubation with CAABE-loaded LSN-1 at two different prodrug equivalent concentrations (0.16 or 0.48 μg mL^{-1}), illumination at 350 nm (2.2 mW cm^{-2}) for 30 or 60 min, and a subsequent rest in the incubator for an additional 72 h.

The neuroblastoma SH-SY5Y cell line showed a significant drop in cell viability at all conditions, consistent with its high sensitivity to CPT cytotoxicity. SH-SY5Y is a noradrenergic cell line and CPT-induced DNA damage is dramatically high; it also exhibits severe repair deficiency.[50] Irradiation with UV light activated CAABE *trans* → *cis* photoswitching, promoting prodrug release and increasing CPT release within cells, but in SH-SY5Y cells only a long exposure time (60 min) and high prodrug loading (0.48 μg mL^{-1}) showed a statistically significant effect. Conversely, in the case of U251 and HeLa cells, cell death induced by photocontrolled release of CAABE was dramatic, and statistically a significant decrease in cell survival was observed after 30 min of photoexcitation even at a low prodrug concentration (0.16 μg mL^{-1}). In the most noticeable case, HeLa cells exposed to CAABE-loaded LSN-1 at a prodrug dose of 0.48 μg mL^{-1} showed reduced viability of approximately 50% after 60 min of irradiation, with a final cell survival of ~30%.

Conclusion

In this study, we have applied the "ship in a bottle" principle to a drug delivery system. By synthesizing photoswitchable prodrugs and precisely tailoring the pore structures of mesoporous silica nanoparticles, drug loading and release was controlled through photoisomerization. This proof-of-concept study was developed in three stages: (i) molecular design and synthesis of a CPT prodrug; (ii) tailoring the pore structure of porous silica nanoparticles for controlled prodrug loading and release; and (iii) *in vitro* validation of the DDS in cancer cells. The azobenzene moiety requires the use of UV light, with lower penetration in tissue efficiency, which has potential at *in vivo* applications over skin cancer. However, irradiation in the UVA-I spectrum has a good safety profile, and it may be possible to treat internal tumors using an endoscope particularly considering the high degree of specificity for this method.

Author contributions

Eva Rivero-Buceta: investigation, writing original-draft, methodology, validation. Mirela E. Encheva: methodology, vali-

dation. Bradley Cech: methodology, validation. Eduardo Fernandez: supervision. Germán Sastre: supervision, investigation, writing original-draft, methodology, validation. Christopher C. Landry: supervision, investigation, writing – original draft, writing – review and editing. Pablo Botella: project administration, supervision, investigation, writing – original draft, writing – review and editing.

Conflicts of interest

The authors declare no competing financial interest.

Acknowledgements

This work was supported by the Spanish Ministry of Science and Innovation (grant number PID2019-111436RB-C21). The authors also acknowledge the Microscopy Imaging Center at the University of Vermont and Dr Victoria Moreno (Centro de Investigación Príncipe Felipe, Valencia, Spain) for her technical support in the *in vitro* studies.

References

1 X. Shan, X. Gong, J. Li, J. Wen, Y. Li and Z. Zhang, *Acta Pharm. Sin. B*, 2022, **12**, 3028–3048.
2 M. J. Mitchell, M. M. Billingsley, R. M. Haley, M. E. Wechsler, N. A. Peppas and R. Langer, *Nat. Rev. Drug Discovery*, 2021, **20**, 101–124.
3 J. Cao, D. Huang and N. A. Peppas, *Adv. Drug Delivery Rev.*, 2020, **167**, 170–188.
4 F. Gao, P. Botella, A. Corma, J. Blesa and L. Dong, *J. Phys. Chem. B*, 2009, **113**, 1796–1804.
5 A. Corma, P. Botella and E. Rivero-Buceta, *Pharmaceutics*, 2022, **14**, 110.
6 J. Ding, J. Chen, L. Gao, Z. Jiang, Y. Zhang, M. Li, Q. Xiao, S. S. Lee and X. Chen, *Nano Today*, 2019, **29**, 100800.
7 J. Chen, Z. Jiang, Y. S. Zhang, J. Ding and X. Chen, *Appl. Phys. Rev.*, 2021, **8**, 041321.
8 M. Vallet-Regí, F. Schüth, D. Lozano, M. Colilla and M. Manzano, *Chem. Soc. Rev.*, 2022, **51**, 5365–5451.
9 V. P. Torchilin, *Nat. Rev. Drug Discovery*, 2014, **13**, 813–827.
10 F. C. Lin, Y. Xie, T. Deng and J. I. Zink, *J. Am. Chem. Soc.*, 2021, **143**, 6025–6036.
11 P. Pan, D. Svirskis, S. W. P. Rees, D. Barker, G. I. N. Waterhouse and Z. Wu, *J. Controlled Release*, 2021, **338**, 446–461.
12 N. K. Mal, M. Fujiwara and Y. Tanaka, *Nature*, 2003, **421**, 350–353.
13 Y. Tao, H. F. Chan, B. Shi, M. Li and K. W. Leong, *Adv. Funct. Mater.*, 2020, **30**, 1–28.
14 N. Aibani, P. F. da Costa, J. Masterson, N. Marino, F. M. Raymo, J. Callan and B. Callan, *J. Controlled Release*, 2017, **264**, 136–144.
15 A. Presa, R. F. Brissos, A. B. Caballero, I. Borilovic, L. Korrodi-Gregório, R. Pérez-Tomás, O. Roubeau and P. Gamez, *Angew. Chem., Int. Ed.*, 2015, **54**, 4561–4565.
16 D. F. Costa, L. P. Mendes and V. P. Torchilin, *Adv. Drug Delivery Rev.*, 2019, **138**, 105–116.
17 T. Zhao, P. Wang, Q. Li, A. A. Al-Khalaf, W. N. Hozzein, F. Zhang, X. Li and D. Zhao, *Angew. Chem., Int. Ed.*, 2018, **57**, 2611–2615.
18 H. Deng, L. Lin, S. Wang, G. Yu, Z. Zhou, Y. Liu, G. Niu, J. Song and X. Chen, *Adv. Mater.*, 2019, **31**, 1–8.
19 C. Yao, P. Wang, X. Li, X. Hu, J. Hou, L. Wang and F. Zhang, *Adv. Mater.*, 2016, **28**, 9341–9348.
20 Y. Zhang, Y. Zhang, G. Song, Y. He, X. Zhang, Y. Liu and H. Ju, *Angew. Chem., Int. Ed.*, 2019, **58**, 18207–18211.
21 J. W. Brown, B. L. Henderson, M. D. Kiesz, A. C. Whalley, W. Morris, S. Grunder, H. Deng, H. Furukawa, J. I. Zink, J. Fraser and O. M. Yaghi, *Chem. Sci.*, 2013, **4**, 2858–2864.
22 G. Das, T. Prakasam, M. A. Addicoat, S. K. Sharma, F. Ravaux, R. Mathew, M. Baias, R. Jagannathan, M. A. Olson and A. Trabolsi, *J. Am. Chem. Soc.*, 2019, **141**, 19078–19087.
23 D. Tarn, D. P. Ferris, J. C. Barnes, M. W. Ambrogio, J. F. Stoddart and J. I. Zink, *Nanoscale*, 2014, **6**, 3335–3343.
24 S. Angelos, Y. W. Yang, N. M. Khashab, J. F. Stoddart and J. I. Zink, *J. Am. Chem. Soc.*, 2009, **131**, 11344–11346.
25 J. Lu, E. Choi, F. Tamanoi and J. I. Zink, *Small*, 2008, **4**, 421–426.
26 T. Kusukawa and M. Fujita, *J. Am. Chem. Soc.*, 1999, **121**(6), 1397–1398.
27 A. Corma and H. Garcia, *Eur. J. Inorg. Chem.*, 2004, **6**, 1143–1164.
28 M. R. Di Nunzio, V. Agostoni, B. Cohen, R. Gref and A. Douhal, *J. Med. Chem.*, 2014, **57**, 411–420.
29 J. Xu, L. Wu, T. Guo, G. Zhang, C. Wang, H. Li, X. Li, V. Singh, W. Chen, R. Gref and J. Zhang, *Int. J. Pharm.*, 2019, **556**, 89–96.
30 S. Lu, D. Tu, X. Li, R. Li and X. Chen, *Nano Res.*, 2016, **9**, 187–197.
31 R. B. Greenwald, A. Pendri, C. D. Conover, C. Lee, Y. H. Choe, C. Gilbert, A. Martinez, J. Xia, D. Wu and M.-M. Hsue, *Bioorg. Med. Chem.*, 1998, **6**, 551–562.
32 J. Fan, C. Yu, J. Lei, Q. Zhang, T. Li, B. Tu, W. Zhou and D. Zhao, *J. Am. Chem. Soc.*, 2005, **127**, 10794–10795.
33 B. Tian, X. Liu, C. Yu, F. Gao, Q. Luo, S. Xie, B. Tu and D. Zhao, *Chem. Commun.*, 2002, **2**, 1186–1187.
34 E. Merino and M. Ribagorda, *Beilstein J. Org. Chem.*, 2012, **8**, 1071–1090.
35 A. Koteja, M. Szczerba and J. Matusik, *J. Phys. Chem. Solids*, 2017, **111**, 294–303.
36 H. M. D. Bandara and S. C. Burdette, *Chem. Soc. Rev.*, 2012, **41**, 1809–1825.
37 K. Ichimura, *Phys. Chem. Chem. Phys.*, 2015, **17**, 2722–2733.
38 L. Huang, X. Yan and M. Kruk, *Langmuir*, 2010, **26**, 14871–14878.
39 P. Horcajada, A. Rámila, J. Pérez-Pariente and M. Vallet-Regí, *Microporous Mesoporous Mater.*, 2004, **68**, 105–109.

40 P. Botella and E. Rivero-Buceta, *J. Controlled Release*, 2017, **247**, 28–54.
41 A. M. Clemments, P. Botella and C. C. Landry, *J. Am. Chem. Soc.*, 2017, **139**, 3978–3981.
42 T. Higuchi, *J. Pharm. Sci.*, 1963, **52**, 1145–1149.
43 F. Li, L. Jin, J. Han, M. Wei and C. Li, *Ind. Eng. Chem. Res.*, 2009, **48**, 5590–5597.
44 E. B. Lim, T. A. Vy and S. W. Lee, *J. Mater. Chem. B*, 2020, **8**, 2096–2106.
45 S. Feles, C. Overath, S. Reichardt, S. Diegeler, C. Schmitz, J. Kronenberg, C. Baumstark-Khan, R. Hemmersbach, C. E. Hellweg and C. Liemersdorf, *Methods Protoc.*, 2022, **5**, 1–14.
46 A. M. Luciani, A. Rosi, P. Matarrese, G. Arancia, L. Guidoni and V. Viti, *Eur. J. Cell Biol.*, 2001, **80**, 187–195.
47 D. W. Lee, M. Y. Lee, B. Ku and D. H. Nam, *J. Biomol. Screening*, 2015, **20**, 1178–1184.
48 P. Botella, I. Abasolo, Y. Fernández, C. Muniesa, S. Miranda, M. Quesada, J. Ruiz, S. Schwartz and A. Corma, *J. Controlled Release*, 2011, **156**, 246–257.
49 R. Mohammadpour, D. L. Cheney, J. W. Grunberger, M. Yazdimamaghani, J. Jedrzkiewicz, K. J. Isaacson, H. Dobrovolskaia and M. A. Ghandehari, *J. Controlled Release*, 2020, **324**, 471–481.
50 Y. Wang, P. R. Musich, K. Cui, Y. Zou and M. Y. Zhu, *Neurotoxic. Res.*, 2015, **27**, 368–383.